IEEE Open Journal of
Antennas and Propagation

Received 4 March 2022; revised 30 March 2022; accepted 10 April 2022. Date of publication 27 April 2022; date of current version 5 May 2022.

Digital Object Identifier 10.1109/OJAP.2022.3170795

Mutual Coupling and Channel Imbalance Calibration of Colocated MIMO Radars

RICARD L. GROVE [1], JØRGEN DALL [1] (Member, IEEE), AND POUL LETH-ESPENSEN [2]

[1] Technical University of Denmark, DTU Space, 2800 Kongens Lyngby, Denmark

[2] Technology & Innovation, TERMA A/S, 8520 Lystrup, Denmark

CORRESPONDING AUTHOR: R. L. GROVE (e-mail: rigr@space.dtu.dk)

This work was supported by the Thomas B. Thriges Foundation.

ABSTRACT The Multiple-Input Multiple-Output (MIMO) radar combines the signals from multiple transmit and receive elements separately to form a virtual array. Consequently, system imperfections in the MIMO radar caused by channel imbalance and mutual coupling are repeatedly present in the virtual array, affecting the beamforming performance. In this paper, the beam pattern deviations caused by these imperfections are described mathematically in relation to a single point target. Furthermore, a nonparametric calibration technique to estimate and compensate for these effects at different angles is presented by exploiting that the same imperfections are present multiple times in the virtual array. The proposed calibration method is applied to measurements with an 8×8 colocated X-band MIMO radar, and the peak sidelobe level (PSL) and the integrated sidelobe level (ISL) are used as performance parameters. The calibration technique is found to improve both the PSL and the ISL by approximately 15 dB within the whole field-of-view (FOV) for antennas that are not minimum scatterers. For angles above $\pm 30^\circ$ from the antenna boresight, the performance of the proposed calibration method is found to surpass other calibration methods. This is advantageous for MIMO radars as they typically cover a wide FOV.

INDEX TERMS Multiple-input multiple-output (MIMO), radar system, calibration, channel imbalance, mutual coupling, colocated, beamforming.

I. INTRODUCTION

IN RELATION to the number of physical elements, the multiple-input and multiple-output (MIMO) radar offers the enhanced angular resolution within a large field-of-view (FOV) and hence new capabilities for multichannel radar systems, including identification and surveillance [1]–[5]. When applying beamforming to the virtual array, system imperfections in a single channel, whether originating from channel imbalance or influence from nearby channels, occur repeatedly since each transmit channel is combined with every receive channel.

Typically, a small element spacing of the virtual array is desired to reduce the angular ambiguities, and inevitably some of the physical antenna elements are located in close proximity. Consequently, these elements are subject to mutual coupling, which has led to a considerable number of studies within the topic on antenna arrays [6]–[9]. In some cases, antenna mutual coupling can be adequately described by a scattering matrix containing the scattering parameters (S-parameters) of the array, or equivalently by embedded element radiation patterns. Early studies describe mutual coupling of phased-array radars, demonstrating a scan angle dependency of the S-parameters. If the element patterns within an array are identical, the total radiated field can be estimated by multiplying with the array pattern without considerable errors [10]. This is typically the case for large arrays with identical elements, even with the presence of mutual coupling where the embedded radiation pattern differs from that of an isolated element. If the element radiation patterns are not identical due to the geometrical array environment, the array pattern multiplication cannot be applied without serious degradation of the system performance. Particularly, the end-elements of linear arrays are highly affected by their asymmetric surroundings, and

instead the measured or computed active element pattern of each element is to be considered, when estimating the total radiated field [11], [12].

In contrast to phased-array radar, a MIMO radar ideally emits orthogonal waveforms from the transmit elements to form the virtual array, such that the total field is not steered towards a specified scan angle. Similarly, each receive element is accessed separately without scanning in a certain angle, which preserves all information for a price of an increased amount of data and system complexity. Hereby, digital beamforming can be applied, and the scattering matrix becomes constant. Nevertheless, depending on the selection of waveforms, the scattering matrix can potentially vary as a function of time as documented for phase-coded waveforms in [13]–[15]. The effects on the beam pattern from system imperfections in a MIMO radar system have been investigated for worst-case boundaries through statistical analysis [16]. Furthermore, mutual coupling effects are analyzed by implementing a MIMO communication model that also considers impedance matching in [17].

Evidently, calibration is required, and several studies have proposed measurement-based calibration methods. By using the measured channel deviations from a single calibration target, decent calibration coefficients are conveniently obtained such as in [4]. The robustness can be increased by measuring the reflected signal from several known targets to estimate more suitable calibration coefficients. It is done either from the relative average amplitude and phase deviation throughout each virtual channel [18] or from the phase slope and offset through a set of linear equations and applying matrix inversion [19]. In general, these methods perform well for calibration of channel imbalance, however, they assume that the effects of system imperfections are angle independent. This is not the case for mutual coupling even if the S-parameters are constant. Without taking this matter into account, the calibration performance often decreases for increasing angles, as the embedded element patterns between the end- and center-elements diverge.

Estimating the direction of targets in presence of mutual coupling is described in [20]–[22] using super-resolution techniques such as MUSIC and ESPRIT. These techniques have high computational complexity and require multiple samples realized by a series of pulses which affects the Doppler domain. A calibration method which applies the coupling matrix from the measured S-parameters is introduced in [14], [23], but the method is not applied to a full MIMO system. This is done in [24], [25] with a least-squares approach, but the method does not utilize that the effect of a physical element impacts several virtual elements. Additionally, the relation between the coupling matrix and the embedded element radiation pattern only applies to minimum scattering antennas (MSA) [26]–[28]. An MSA assumes that the scattering of an antenna under matched conditions, referred to as residual or structural scattering, has a pattern identical to that of the element, which is typically not the case. Furthermore, even if the antennas were minimum scatterers, they would not necessarily behave as such, e.g., if the surrounding environment also affects the elements. Finally, mutual coupling can also occur within the RF system. For MIMO radar systems using an RF mixing stage, the use of a shared local oscillator may lead to RF mutual coupling through the power splitters.

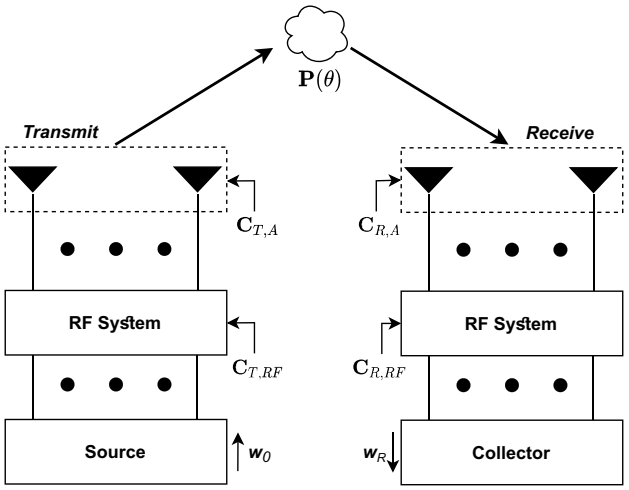

FIGURE 1. Block diagram representation of a MIMO radar signal model including channel imbalance and mutual coupling from generation of ideal waveforms to collection of the received imperfect signals.

In this paper, a calibration method to compensate for channel imbalance and mutual coupling is proposed using several observations of the relative radiation pattern obtained within a single MIMO measurement. As such a measurement includes all system errors, this method performs well even if the antenna elements are not MSAs, corrects for impedance mismatch, and takes the potential environment effects on the elements into account. In the following section, a system level model including channel imbalance and mutual coupling is presented with appropriate assumptions.

Section III describes some calibration considerations, emphasizing the importance to calibrate for both the mutual coupling and channel imbalance. These considerations motivate the proposed method, which is described in Section IV. Here an X-band MIMO system with colocated elements is used to document the increased calibration accuracy of the proposed calibration technique.

II. SIGNAL MODEL

A block diagram of a MIMO radar signal model including system imperfections is illustrated in Fig. 1, where the different contributions to imperfections are separated. It forms the basis of the signal model described in the following. The derivation of the model reflects the signal path, and it is hence divided into a transmission, propagation, and reception section.

A. TRANSMISSION

Initially, a source generates the number of ideally orthogonal waveforms corresponding to the number of transmitters, N_T.

In the absence of noise, the waveforms can be written as

$$\boldsymbol{w}_0(t) = \left[w_1(t), w_2(t), \ldots, w_{N_T}(t)\right]^T, \tag{1}$$

where $(^T)$ denotes the transpose and $w_i(t)$ is the time-varying signal of channel i. As the signals traverse through the different components in the RF system, undesired amplitude and phase variations across the channels occur, which is also referred to as channel imbalance. These effects can be described by a diagonal square matrix of order N_T:

$$\mathbf{C}_{T,RF} = \begin{bmatrix} c_{11} & 0 & \cdots & 0 \\ 0 & c_{22} & \ddots & 0 \\ \vdots & \ddots & \ddots & \vdots \\ 0 & 0 & \cdots & c_{N_T N_T} \end{bmatrix}, \tag{2}$$

where the c_{ii} is the complex channel imbalance coefficient of element i. For the purpose of this paper, it is assumed that there is no RF mutual coupling, which otherwise would be included in the off-diagonal elements in (2). As the generated signal reaches the antenna elements, the presence of adjacent elements will additionally lead to scattering, which can be described by the square coupling matrix of order N_T

$$\mathbf{C}_{T,A} = \frac{1}{\sqrt{Z_T}} \left(\mathbf{I}_{N_T} - \begin{bmatrix} S_{11} & S_{12} & \cdots & S_{1N_T} \\ S_{21} & S_{22} & \ddots & S_{2N_T} \\ \vdots & \ddots & \ddots & \vdots \\ S_{N_T 1} & S_{N_T 2} & \cdots & S_{N_T N_T} \end{bmatrix} \right), \tag{3}$$

where Z_T is the termination impedance or reference impedance, S_{ij} describes the S-parameter from the excited channel j to channel i, and $\mathbf{I}_{N_T}$ is the identity matrix of order N_T. The diagonal elements of the scattering matrix in (3) are known as the reflection coefficients, whereas the off-diagonal elements are the antenna mutual coupling coefficients. The characteristics of the antenna mutual coupling depend on the antenna type, the array geometry and antenna orientation. By combining (2) and (3), an imperfection matrix for the transmit array can be described as

$$\mathbf{C}_T = \mathbf{C}_{T,A}\mathbf{C}_{T,RF}, \tag{4}$$

which is a square matrix of order N_T. For an ideal system the imperfection matrix equals the identity matrix: $\mathbf{C}_T = \mathbf{I}_{N_T}$. In (4) it is assumed that the system is frequency independent throughout the entire signal bandwidth, which is typically the case for narrowband signals.

B. PROPAGATION

After transmission, the signals propagate from the transmitting elements, and reflections from targets and clutter will be collected by the N_R receiving elements. For a point target, the resulting signal is described by the channel matrix

$$\mathbf{P}(r,\theta,\phi) = \mathbf{E}_R(\theta,\phi)\mathbf{A}(r,\theta,\phi) \odot \exp\left[-jk\mathbf{T}(r,\theta,\phi)\right]\mathbf{E}_T(\theta,\phi), \tag{5}$$

where $\odot$ is the Hadamard product, i.e., the elementwise multiplication, $\exp[\,\cdot\,]$ denotes the elementwise exponential, k is the wave number, while $\mathbf{E}_R$ and $\mathbf{E}_T$ are square diagonal matrices of order N_R and N_T, respectively. They correspond to the isolated element patterns of the receive and transmit array elements for the given direction angle in azimuth, θ, and elevation, ϕ, measured from the normal to the plane of the MIMO system antenna constellation. $\mathbf{A}$ is the $N_R \times N_T$ attenuation matrix describing the propagation attenuation as the signal propagates from each transmitter to every receiver, including the radar cross section of the target at range r. Similarly, $\mathbf{T}$ is the $N_R \times N_T$ matrix describing the phase change due to the signal propagation as a function of the receive and transmit element position and the target position, assuming a propagation speed equal to the speed of light. Thus, the channel matrix $\mathbf{P}$ represents the ideal system without imperfections.

Depending on the application for the model, several simplifications can be made, which will also be the case here. First, it is assumed that the transmit and receive array are parallel such that the elevation angle, ϕ, can be omitted. Next, the target is assumed a single point target in the far-field of the array with identical radar cross section for all N_T transmitted signals such that $\mathbf{A}$ can be ignored. Finally, it is assumed that the system is colocated such that the direction-of-arrival (DOA) angle is identical for all elements. Hereby, $\mathbf{T}$ can be split in two phase-terms. First a constant phase-term by the two-way propagation path from a reference point on the MIMO array, which can be ignored. Second, a relative phase change due to the array element positions, which is of interest for direction estimation [29]. Disregarding the element patterns, the amplitude-normalized channel matrix becomes

$$\mathbf{P}(\theta) \cong \exp\left[-jk\sin(\theta)\boldsymbol{y}\right]\exp\left[-jk\sin(\theta)\boldsymbol{x}^T\right], \tag{6}$$

with $\boldsymbol{x}$ and $\boldsymbol{y}$ being the position vectors describing the relative distance of each element in the azimuth direction of the transmit and receive array, respectively

$$\boldsymbol{x} = \left[x_1,\ x_2,\ \ldots\ ,\ x_{N_T}\right]^T, \tag{7}$$

$$\boldsymbol{y} = \left[y_1,\ y_2,\ \ldots\ ,\ y_{N_R}\right]^T, \tag{8}$$

such that $\mathbf{P}(\theta)$ becomes an $N_R \times N_T$ matrix.

C. RECEPTION

Similar to the transmit array, mutual coupling in the receive array also occurs together with channel imbalance, which again is implemented by a square matrix, $\mathbf{C}_R$, of order N_R. It should be noted that on transmit side the channel imbalance of the RF system occurs prior to the antenna mutual coupling, and in the opposite order on the receive side. Combining (1), (4) and (6), the signal collected on the receive side as seen in Fig. 1, can then be described as

$$\boldsymbol{w}_R(t,\theta) = \mathbf{C}_R\mathbf{P}(\theta)\mathbf{C}_T\boldsymbol{w_0}(\mathrm{t}) + \boldsymbol{e}(t), \tag{9}$$

such that $\boldsymbol{w}_R$ becomes a column vector with N_R elements, and $\boldsymbol{e}(t)$ is the noise vector with independent Gaussian white noise consisting of N_R elements as well.

The virtual antenna array is formed by cross-correlating the collected signals at each receiver in $\boldsymbol{w}_R(t,\theta)$, with a copy of all transmitted waveforms in $\boldsymbol{w}_0$(t), also referred to as matched filtering. Assuming that the transmitted signals are orthogonal, the normalized matched filter output will be one. It is also assumed that range migration is negligible (or corrected for), i.e., the line-of-sight dimension of the array is much less than the range resolution. From (9), the maximum normalized matched filter output, including imperfections, becomes

$$\mathbf{W}_{out}(\theta) = \mathbf{C}_R\mathbf{P}(\theta)\mathbf{C}_T + \varepsilon, \tag{10}$$

with $\mathbf{W}_{out}(\theta)$ being another $N_R \times N_T$ matrix, and ε being the normalized additive noise matrix. As the noise in (10) is added posterior to matched filtering, the SNR is typically increased equal to the pulse-compression ratio compared to the additive noise in (9). Depending on the MIMO array configuration, direct coupling between the transmit and receive elements can occur. It is a rather simple operation to mask out this coupling after matched filtering, because the signal will be at near-zero range. Nevertheless, the propagation loss is near-zero for the direct coupling between the transmit and receive elements, such that even low coupling coefficients can saturate the system or increase the sidelobe level from imperfect waveform orthogonality. This can become critical for especially coded waveforms, where the sidelobe level is restricted by the cross-correlation between the waveforms.

If the imperfection matrices have been estimated, the ideal signal output can easily be computed by multiplication of the inverse of the transmit and receive imperfection matrices

$$\mathbf{W}_{cal}(\theta) = \mathbf{C}_R^{-1}\mathbf{W}_{out}(\theta)\mathbf{C}_T^{-1}, \tag{11}$$

which leads to a calibrated system. In principle, $\mathbf{C}_R$ and $\mathbf{C}_T$ can be ill-conditioned, but diagonally dominant matrices are often well-conditioned such that the inverse can be estimated. The challenge is of course to obtain the calibration matrix either by simulations or measurements, such that the effects of the imperfections are minimized.

III. CALIBRATION CONSIDERATIONS

The presented system model can be applied to all array configurations. In this paper, a common MIMO system is however assumed; one array consists of a uniform linear array (ULA) with $\lambda/2$ spacing, d_F, where λ is the free space wavelength, and the subscript "F" refers to the array being full. This array has also been referred to as a standard linear array (SLA), because the maximum element distance is achieved without forming any angular grating lobes when performing beamforming. The second array in the MIMO system is a ULA with a spacing of $d_S = N_F d_F$, where the subscript "S" refers to array being sparse. In the following, this MIMO system will be addressed as a standard MIMO array (SMA), since an $N_F \times N_S$ SMA forms a virtual SLA array with $N_F N_S$ elements. For such a system it is necessary to vectorize the output matrix prior to beamforming.

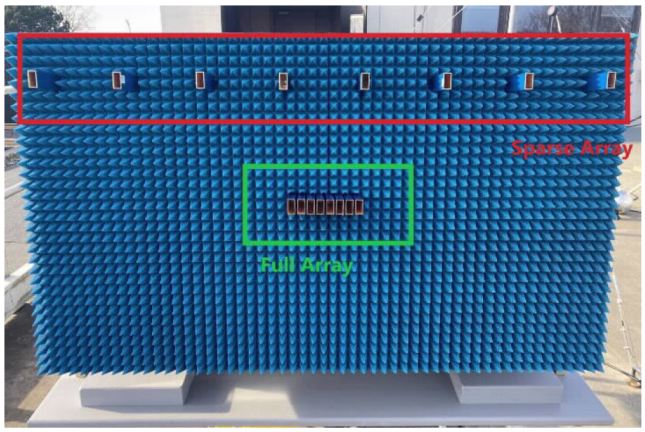

FIGURE 2. The experimental X-band MIMO array, designed and constructed at DTU Space, used for calibration verification, and consisting of a sparse and full array of open-ended waveguide antennas.

It can be expressed as

$$\boldsymbol{w}_{out}(\boldsymbol{\theta}) = \mathrm{vec}(\mathbf{W}_{out}(\theta)), \tag{12}$$

with vec(·) denoting the vectorization, which converts a matrix to a column vector through a linear transform by stacking the columns. Furthermore, it should be noted that if the array of transmitters represents the full array, a transpose of $\mathbf{W}_{out}(\theta)$ is required prior to vectorization. Otherwise, the vectorization will stack the virtual elements from each sparse element consecutively instead of the full array, resulting in nonconsecutive spatial sampling of the virtual array.

In the following, three calibration considerations are described. The simulations that exemplify the considerations will build on an X-band SMA system as illustrated in Fig. 2, which is also used to demonstrate the proposed calibration technique experimentally. The system consists of commercial off-the-shelf components, features transmission of arbitrary waveforms with adjustable data collection up to 4 GB, and has its bandwidth limited to 200 MHz due to the RF subsystem. The antenna elements of the MIMO system are standard WR90 open-ended waveguides with $N_F = N_S = 8$ with a sufficient length to attenuate higher modes in the waveguide. Open-ended waveguides are suitable for a MIMO radar due to their broad element pattern, which allows a large FOV. Additionally, absorbers surrounding the elements are added to reduce backlobe reflections, which will also affect the embedded element radiation pattern.

Fig. 3 illustrates a model of the full array of the experimental MIMO radar for computational electromagnetics (CEM) using CST Microwave Studio. A transient solver is used to simulate the scattering matrix depicted in Fig. 4, and the element radiation patterns to investigate the antenna mutual coupling effects. Since the mutual coupling is highly related to the element spacing relative to λ, its influence on the sparse array will depend on N_F for an SMA, such that antenna mutual coupling can be neglected for large arrays. In this specific case with open-ended waveguides and $N_F = 8$, the simulated coupling was found to be below -30 dB for

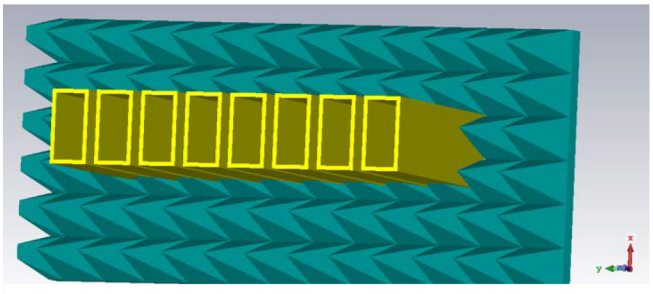

FIGURE 3. Full array model of the experimental MIMO system applied in a full-wave simulator.

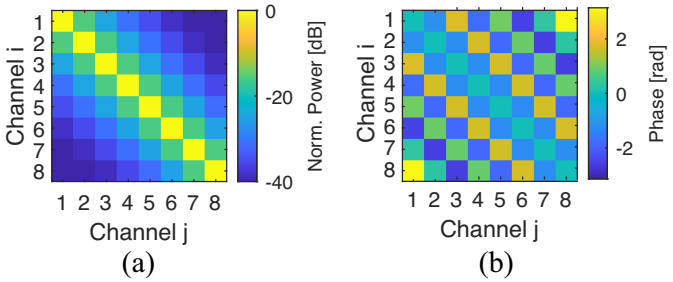

FIGURE 4. Normalized amplitude (a) and phase (b) of the modelled S-parameters estimated from the model in Fig. 3.

the sparse array even without the surrounding absorbers. Hence, the sparse array has a relatively small influence on the mutual coupling in the system.

A. MINIMUM SCATTERING ANTENNA

When calibrating for antenna mutual coupling using S-parameters, it is assumed that the antenna array consists of MSAs. For an antenna element, the absorption efficiency is defined as [28]

$$\eta = \frac{1}{2}\left(1 - \sqrt{1 - \frac{D_a}{D_s}}\right), \tag{13}$$

where D_a and D_s are the element directivity and scattering directivity, respectively. For an MSA, an equal amount of received energy is absorbed and scattered such that $\eta = 0.5$ with a thin dipole being the most common example of an MSA. The coupling matrix for an MSA with respect to impedance can be described as [27]

$$\mathbf{C}_A = (Z_T + Z_A)(\mathbf{Z} + Z_T\mathbf{I}_N)^{-1}, \tag{14}$$

with Z_T being the reference impedance, and Z_A being the antenna impedance computed from [30]:

$$Z_{A,n} = Z_{T,n}\left(\frac{1 + S_{nn}}{1 - S_{nn}}\right), \tag{15}$$

where S_{nn} is the diagonal element n of the scattering matrix, such that $Z_A = Z_T$ in the case of complex conjugated impedance matching. Finally, $\mathbf{Z}$ is the mutual impedance matrix described by [30]

$$\mathbf{Z} = Z_T(\mathbf{I}_N + \mathbf{S})(\mathbf{I}_N - \mathbf{S})^{-1}, \tag{16}$$

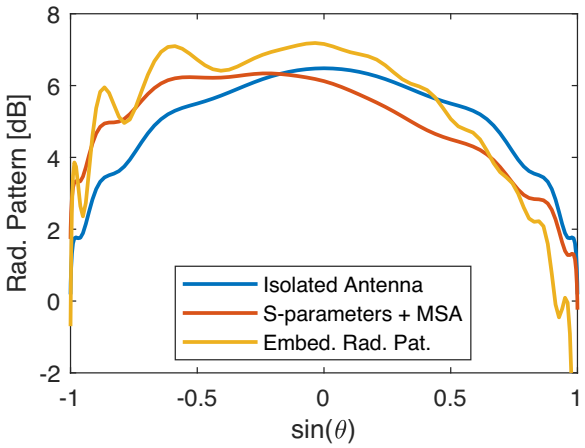

FIGURE 5. Comparison of element radiation patterns of an isolated open-ended waveguide from a CEM model, an end-element of the array model estimated from the obtained scattering parameters, and directly from the CEM model. For consistency, all models are without surrounding absorbers.

where $\mathbf{S}$ is the scattering matrix. For most systems, $\mathbf{S}$ can be measured with a Vector Network Analyzer, and the reference impedance, Z_T, is generally 50 Ω.

For MSAs, the array radiation pattern is a function of the mutual impedance [27]:

$$E(\theta) = E_{iso}(\theta)\boldsymbol{a}_\mathbf{s}(\theta)(\mathbf{Z} + Z_T\mathbf{I}_N)^{-1}\boldsymbol{v}, \tag{17}$$

where $E_{iso}(\theta)$ is the element pattern of an isolated element and $\boldsymbol{a}_\mathbf{s}$ is the so-called steering vector using an end-element as reference:

$$\boldsymbol{a}_\mathbf{s}(\theta) = \left[1 \mathrm{e}^{-jkd\ sin(\theta)} \cdots \mathrm{e}^{-jkd(N-1)sin(\theta)}\right], \tag{18}$$

where d is the distance between the elements. In (17), $\boldsymbol{v}$ is a column vector of the generator voltages or open circuit voltages, if referring to either a transmitting or receiving array. Considering only the embedded element pattern of a single element such that all other elements are terminated, the unit voltage array becomes

$$V_{0q}^{(p)} = \begin{cases} 0, & \text{if } p \neq q \\ V_0 = 1 & \text{if } p = q, \end{cases} \tag{19}$$

when evaluating element q and exciting element p. Combining (19) and (17), it is thus possible to compute the embedded radiation pattern from the isolated element pattern and the scattering matrix assuming minimum scatterers.

Fig. 5 illustrates the radiation patterns of three different scenarios similar to the modelled array in Fig. 3, but without the surrounding absorbers. First, the isolated radiation pattern which has a symmetric amplitude around boresight. Second, the embedded radiation pattern of an end-element estimated from the CEM scattering matrix using the MSA approximation (17) with all other elements terminated. Third, the embedded radiation pattern estimated with the same CEM again with sequential excitation. It is obvious, that the embedded radiation pattern from the minimum scattering approximation is not identical to the simulated pattern, and

consequently, the calibration performance of mutual coupling is degraded when assuming MSAs. Since the antenna array of open-ended waveguides has a small airgap between each element, it is not considered an MSA, as the absorption efficiency was estimated to be about 0.25 [28]. Furthermore, in the specific case with surrounding absorbers as illustrated in Fig. 2 and Fig. 3, the radiation pattern is additionally altered, such that the behavior of the antennas further deviates from minimum scatterer condition. This is not necessarily undesired, as the absorbers are found to smooth the radiation pattern for especially larger angles. Without the gaps between the elements, the array would become a slot-type antenna, which is an example of an MSA with respect to admittance [27].

Fig. 5 only addresses antenna mutual coupling, but as mentioned mutual coupling can also occur in the RF subsystem. Assuming only a single element being excited, the passive elements will additionally radiate an attenuated and phase shifted copy of the generated signal, depending on the path length deviation in the RF subsystem. Independently of the antenna type, the resulting embedded radiation patterns will deviate from the radiation patterns that are estimated from the S-parameters.

B. EMBEDDED RADIATION PATTERN

Large arrays are often assumed to be infinite, omitting the effects of the end-elements, where the embedded element patterns differ from the center-elements due to the asymmetric array environment. However, for an SMA MIMO system, the impact of mutual coupling on the end-elements of the full array will repeat itself periodically N_S times through the virtual array. The resulting sidelobes will have their power concentrated in N_S equidistant peaks in the angular frequency domain as described in [31]. Naturally, the effect also decreases with an increasing number of elements, since the percentage of virtual elements affected decreases assuming $N_F = N_S$.

Fig. 6 illustrates the simulated normalized power of the beam pattern using a Fast Fourier Transform (FFT) of (12). A relative amplitude deviation of 4 dB of an end-element in the full array is assumed, omitting the small phase deviation due to a change of the element phase center. Hence, mutual coupling is also disregarded in this example, resulting in the following diagonal imperfection matrix of the full array

$$\mathbf{C}_{F,nn} = \begin{cases} 1.6 & \text{if } n = 1 \\ 1 & \text{otherwise,} \end{cases} \tag{20}$$

for element n. The applied amplitude deviation corresponds to the embedded radiation pattern measured with the MIMO system seen in Fig. 2, which is illustrated in Section IV. The virtual array has been Hamming weighted resulting in an ideal maximum sidelobe level of -42.5 dB. Weighting has been applied, because an unweighted system has very few practical uses due to the high sidelobe levels. With a system of eight elements in the full and sparse array, the sidelobe level has risen to about -23 dB, whereas with sixteen elements the sidelobe level is about -29 dB, which is still significantly higher than the Hamming weighted sidelobe level. Of course, the change of the sidelobe levels depends on the window function since the ratio of the system error magnitude and sidelobe level plays a significant role. Hence, for a Dolph-Chebyshev window with a theoretical sidelobe level of -30 dB, the maximum sidelobe level of 8×8 and 16×16 SMAs would be -20 dB and -23 dB, respectively. Therefore, the impact of the channel imbalance caused by the embedded radiation patterns of the end-elements, cannot be ignored even for large systems. Additionally, if the array is not an MSA as shown previously, the correction of the element pattern will not yield optimal beamforming results.

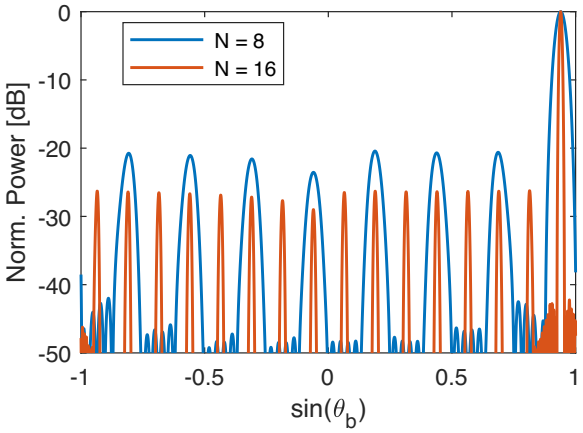

FIGURE 6. Simulated SMA system beam pattern for an 8 × 8 and 16 × 16 SMA system with a target at $\theta_0 = 70°$. An amplitude deviation of 1.6 of an end-element in the full array is assumed with θ_b indicating the beamforming angle.

C. COMBINED CHANNEL IMBALANCE AND MUTUAL COUPLING

From (4), it is seen that the imperfection matrix is a combination of channel imbalances and mutual coupling. In principle, it is possible to correct for the two imperfection effects independently, but depending on the RF system, it is either not possible or cumbersome to calibrate for channel imbalance without calibration of mutual coupling. If the antenna array consists of MSAs, the mutual coupling can be compensated for directly from obtained S-parameters, followed by a calibration of the channel imbalance. Nonetheless, the minimum scattering assumption does not apply to many antenna arrays. Another problem arises when only one of the two imperfections are considered, because they can either affect each other constructively or destructively, such that a calibration of only one of the imperfections potentially yields a worse outcome.

Fig. 7 and Fig. 8 illustrate the Hamming-weighted beam pattern for three different imperfection scenarios for an 8×8 SMA. For all scenarios, a point target is located at boresight, i.e., $\theta_0 = 0$, and it is assumed that the sparse array is ideal. Each curve in both figures has been normalized

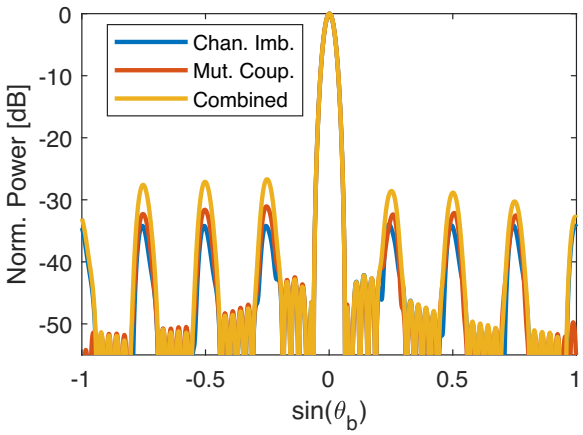

FIGURE 7. Normalized simulated 8 × 8 MIMO radar beam pattern with an imbalanced channel of −0.15 radians, causing constructive interference.

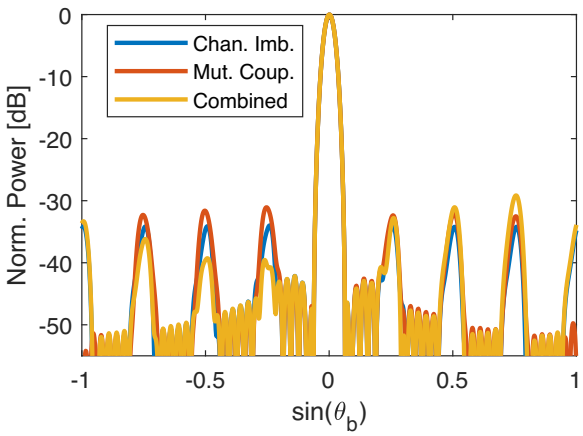

FIGURE 8. Normalized simulated 8 × 8 MIMO radar beam pattern with an imbalanced channel of 0.15 radians, causing destructive interference.

to its maximum value, instead of the ideal array, since the relative sidelobes are the ones of interest. First, no mutual coupling is present, but a channel imbalance of 0.15 radians is applied to the first channel of the full array similar to (20) but with $\mathbf{C}_F(1,1) = 0.9888 \pm 0.1494\mathrm{i}$. Second, mutual coupling is applied assuming no channel imbalance using the S-parameters from Fig. 4, and finally the combined channel imbalance and mutual coupling is applied as described above. The channel imbalance and mutual coupling separately increases the sidelobe level, but when the imbalance is −0.15 as in Fig. 7, the phase of the imperfections will add up constructively in accordance with the matrix multiplication in (10), since the S-parameter of the neighboring element has a negative phase. This element has the highest contribution to the beam pattern deviations due to the high amplitude. Hereby the resulting sidelobe level further increases, and a calibration of either channel imbalance or mutual coupling improves the beamforming performance. This is opposite in Fig. 8, where the channel imbalance phase is positive, such that the imperfections add destructively. Consequently, the sidelobe levels for some of the angular frequencies are greatly reduced.

Conclusively, when a system is affected from both channel imbalance and mutual coupling, but only one of these imperfections is corrected for, the system performance can be degraded.

IV. MIMO RADAR SYSTEM CALIBRATION

It is evident, that several aspects of system imperfections in a MIMO radar system are to be considered to increase the performance in the angular dimension of the radar system.

A. PROPOSED CALIBRATION TECHNIQUE

With only a single measurement, several estimates of deviations from an ideal system can be obtained for each channel. This is possible, since $N_R N_T$ virtual elements are formed from only $N_R + N_T$ physical elements, such that an over-determined solution can be formed. However, as described in Section III, the effects of mutual coupling changes with respect to the DOA. Hence, a set of measurements of a calibration target with a MIMO system at different DOA angles is required to achieve high calibration performance for large angles. This can be attained either by rotation of the radar system or by changing the location of the target. For each angle, a set of transmit and receive calibration coefficients are estimated and used for calibration. In this way, they correct for all imperfection effects at a given angle including mutual coupling and presence of the surrounding environment with the price of having angular-dependent calibration coefficients, which increases the computational complexity. Thereby, the measurements should ideally cover the whole FOV, where the angular step-size determines the quantity of estimated calibration coefficient sets. In principle, this is a question of computational complexity on one hand and system performance on the other, as additional sets of calibration coefficients offer better calibration performance. Furthermore, a relatively high SNR is needed, as no averaging is performed between measurements. However, calibration scenarios are in general set up to ensure a strong return signal.

The steps for estimating the calibration coefficients are illustrated in Fig. 9. Starting with a single measurement, the matched filtering in range is applied to the collected signals. Considering only the range bin of the calibration target, the matrix $\mathbf{W}_{out}$ is obtained from (10), where each row represents a receive element and each column a transmit element. Next, the angle-dependent linear phase-term originating from the channel matrix in (6) is removed assuming a target in the far-field or applying a corresponding near-field phase compensation:

$$\mathbf{W}_{res}(\theta) = \mathbf{W}_{out}(\theta) \oslash \mathbf{P}(\theta), \tag{21}$$

with $\oslash$ denoting the Hadamard division. The remaining signal, $\mathbf{W}_{res}(\theta)$, now corresponds to the $N_R \times N_T$ matrix containing the residual signals of all virtual elements for a given angle. Hence, it is not possible to distinguish between

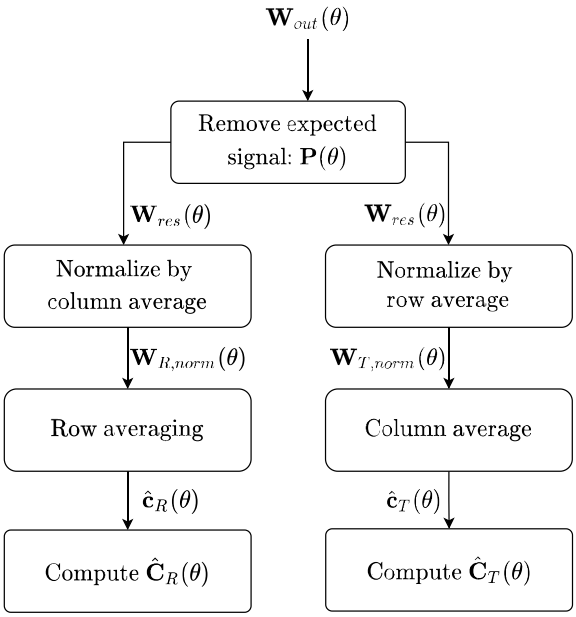

FIGURE 9. Diagram for estimating the calibration coefficients from the proposed calibration method.

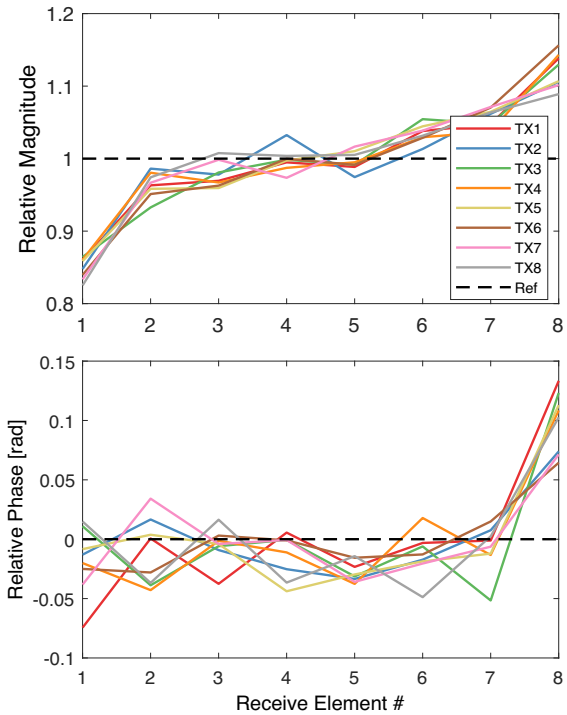

FIGURE 10. Simulated deviations in amplitude (top) and phase (bottom) caused by the receive array mutual coupling for a target at $\theta_0 = 50°$ and SNR of 30 dB.

the different origins of the signal deviations of the virtual elements. Under the assumption that the imperfections affecting each of the $N_R + N_T$ physical elements are constant, the virtual elements can be combined. Starting with the receive array, each column of $\mathbf{W}_{res}(\theta)$ is normalized by its mean value

$$\mathbf{W}_{R,norm}(\theta) = \mathbf{W}_{res}(\theta)\text{diag}\left(\overline{\mathbf{W}}_{res}(\theta)\right)^{-1}, \tag{22}$$

with $\overline{(\cdot)}$ denoting the column average and diag($\boldsymbol{x}$) the diagonal matrix with the vector $\boldsymbol{x}$ as diagonal. Hereby, for each receive channel, N_T estimates of the calibration coefficients are obtained such that $\mathbf{W}_{R,norm}(\theta)$ is another $N_R \times N_T$ matrix. Since each column has been normalized, the deviations due to transmit imperfections are removed, resulting in N_T estimates of the receive imperfections. An example of $\mathbf{W}_{R,norm}(\theta)$ for an 8×8 MIMO system is illustrated in Fig. 10 using the simulated S-parameters from Fig. 4 for the receive array assuming no other imperfections. An interesting observation can be seen for the end-elements, whose amplitude and phase deviate from the mean values. Across the receive elements, opposite tendencies are observed in particular for the amplitude, which is expected due to the array geometry and $\theta_0 = 50°$. In this way, the mutual coupling effects can be considered directly as a channel amplitude and phase deviation for a given angle. These values are finally averaged to estimate the calibration coefficients of the receive array:

$$\widehat{\mathbf{c}}_R(\theta) = \overline{\overline{\mathbf{W}}}_{R,norm}(\theta), \tag{23}$$

with $\overline{\overline{(\cdot)}}$ denoting the row average resulting in a column vector with N_R elements. Hence, these calibration coefficients represent the total imperfection (imbalance and mutual coupling) of the receive channels at a given angle. An imperfection matrix of the receive array can then be formed from

$$\widehat{\mathbf{C}}_R(\theta) = \text{diag}(\widehat{\boldsymbol{c}}_R(\theta)), \tag{24}$$

which is an angle-dependent counterpart of $\mathbf{C}_R$ found in (9) with all contributions of system imperfections gathered in the diagonal. The counterpart of the transmit imperfection matrix $\mathbf{C}_T$ from (4) can be estimated in a similar manner from (22)-(24) by applying averaging in the opposite dimension. Hence, in (22) and (23) the row and column averaging, respectively, is applied to achieve $\widehat{\mathbf{C}}_T(\theta)$ as illustrated in Fig. 9. With $\widehat{\mathbf{C}}_R(\theta)$ and $\widehat{\mathbf{C}}_T(\theta)$ being diagonal matrices, they are not ill-conditioned, and the inverse can be determined. Finally, the system is then calibrated as from (11), followed by beamforming on the resulting virtual array.

In the following, the proposed method will be compared to the calibration method described in [18], where the calibration coefficient of each virtual element is estimated from the average of several measurements at different DOA angles, again with the linear, DOA-related phase-term removed. This method will in the following be referred to as the average-method.

B. EXPERIMENTAL RESULTS

As mentioned in Section III, an SMA radar system is used to demonstrate the calibration technique. The antenna array configuration is illustrated in Fig. 2, and naturally the full array will to a larger extent be influenced by mutual coupling

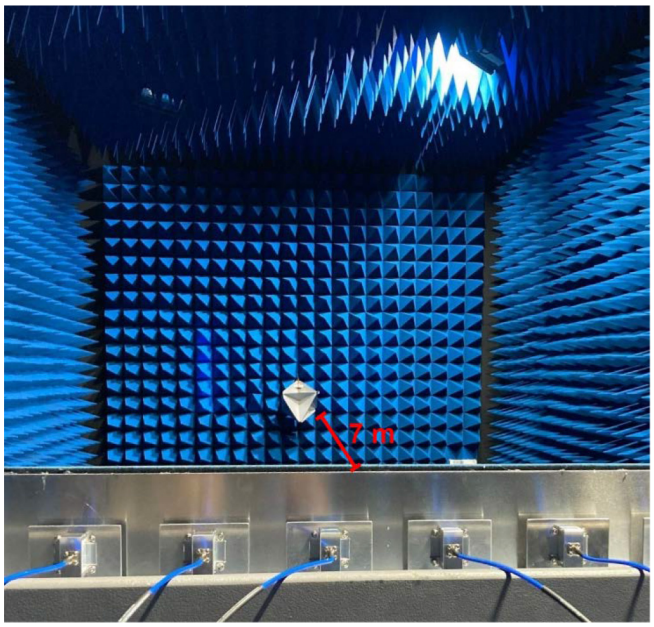

FIGURE 11. Measurement setup in the anechoic chamber from the point of view of the radar system with the calibration target located at boresight.

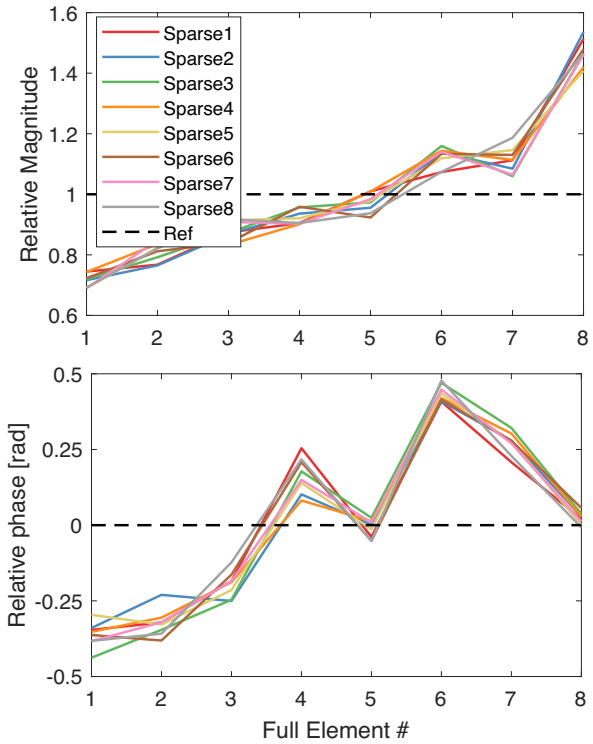

FIGURE 12. Measured amplitude (top) and phase (bottom) for a target at $\theta_0 = 70$ degrees for the transmit array constituting the full array of the SMA.

compared to the sparse array. Nevertheless, the proposed method is nonparametric, i.e., it can be applied to any array configuration. The system was put on top of a turntable, where measurements were performed in the angle interval of $\pm 70°$ from boresight with $1°$ interval. From simulations the open-ended waveguides were found to have a half-power beamwidth of $110°$, such that the resulting FOV of $140°$ covers the scene of interest. If clutter is present during the calibration of the system, this will naturally affect the calibration coefficients, resulting in a degraded performance if the scene changes. Hence, the measurements were conducted in an anechoic chamber to reduce the amount of clutter.

The calibration target was a corner reflector with an RCS of 2.2 dBsm, located in the far end of the chamber at a distance of approximately 7 meters from the system as illustrated in Fig. 11. Since the distance to the target is within the near-field of the system, a near-field phase correction was applied to the data before estimating the calibration coefficients. Additionally, background subtraction has been applied to further reduce the clutter level. This was implemented by simply subtracting the raw data without the calibration target, from those with the calibration target at an angle-to-angle basis. To accommodate the assumption of orthogonal waveforms and avoid time-variant scattering parameters time-division multiplexing, TDM, is selected, where only a single transmitter is radiating at a time. Linear Frequency-Modulated (LFM) waveforms are used to achieve pulse-compression where the full array is used for transmission and the sparse array for reception.

An example of the amplitude and phase values of $\mathbf{W}_{T,norm}(\theta)$ with a calibration target at $\theta_0 = 70°$ is illustrated in Fig. 12. The results are relative to the average values, and the final result is found by averaging over all sparse elements. It is seen that the amplitude of the end-elements has a relative high amplitude deviation, which is expected due the embedded radiation patterns. Since the propagation phase is removed, the relative phase differences mainly arise from channel imbalances and deviations in the phase centers due to the antenna mutual coupling, in particular for the end-elements. Smaller, seemingly random, deviations are seen in both amplitude and phase caused mainly by system noise. Compared to Fig. 10, it is evident that the mutual coupling in the presented MIMO system is stronger than the modelled coupling, as the same trend is observed just with higher variation from the average value.

Fig. 13 illustrates the normalized beam patterns for three different calibration scenarios at boresight and at $\theta_0 = 70°$. The first scenario is the single point target response for the uncalibrated system, the second scenario when applying the proposed calibration method, and the third scenario when applying the average-method in [18]. At boresight, the sidelobe level is clearly reduced for both calibration methods. This is also expected, since the mutual coupling effects at larger angles to some degree cancel out, assuming that the embedded radiation patterns between the two end-elements in the full array are typically mirrored. Furthermore, the sidelobes that do appear are seemingly located periodically, indicating that small channel deviations still occur. It should be noted, that with a very low sidelobe level even

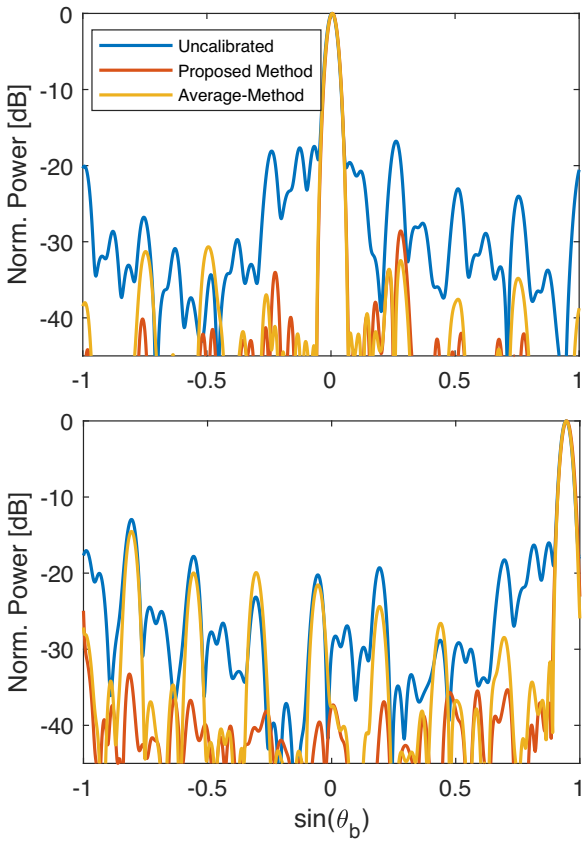

FIGURE 13. Normalized beam pattern with the 8 × 8 MIMO radar when uncalibrated, calibrated with the proposed method, and with the average-method at boresight (top) and at $\theta_0 = 70°$ (bottom).

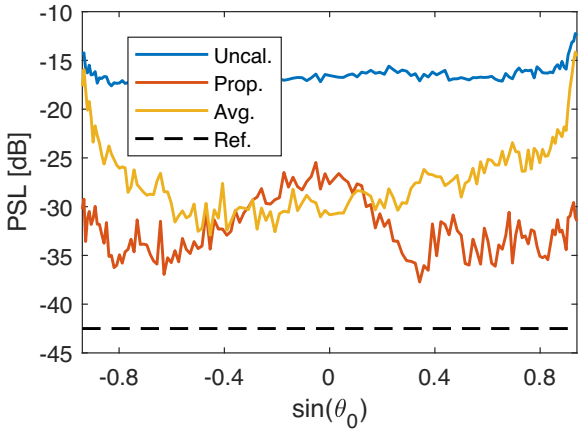

FIGURE 14. PSL for the uncalibrated system, when applying the proposed and average-method, and for a Hamming weighted ideal point target response.

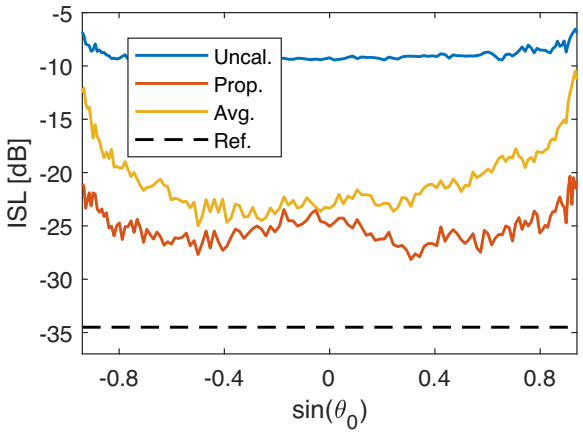

FIGURE 15. ISL for the uncalibrated system, when applying the proposed and average-method, and for a Hamming weighted ideal point target response.

small imperfections will have a relatively high impact on the sidelobes.

At $\theta_0 = 70°$, large sidelobes occur for the uncalibrated system mainly because of the embedded radiation patterns. The average-method does not correct for this effect efficiently, even though the sidelobe level between the peaks is significantly decreased. On the other hand, the proposed method corrects for these effects, resulting in a more constant sidelobe level throughout the whole beam pattern.

To assess the performance of the calibration technique in combination with FFT beamforming, two performance parameters are used, namely the peak sidelobe level (PSL) and the integrated sidelobe level (ISL). The PSL converted to dB is simply computed as

$$\mathrm{PSL} = 20\log_{10}\left(\frac{\max(|\mathrm{SLL}|)}{\max(|\mathrm{MLL}|)}\right), \tag{25}$$

with SLL being the sidelobe level, and MLL the mainlobe level. ISL is calculated as the ratio between the energy within the mainlobe and the sidelobes

$$\mathrm{ISL} = 10\log_{10}\left(\frac{\sum(|\mathrm{SLL}|^2)}{\sum(|\mathrm{MLL}|^2)}\right), \tag{26}$$

where the border between main lobe and sidelobe is at the first null from the main lobe, i.e., where the first local minimum is found. The deviation of the DOA estimation before and after system calibration is below 0.1° for all angles, which is also below the angular resolution of the radar system and will not be assessed further in this paper. However, it is important to notice that the DOA error is to be considered for MIMO radar systems with few elements. In [17] it was found that a 2x4 MIMO radar system had an angle deviation up to 1° for large angles.

Fig. 14 and Fig. 15 illustrate the performance parameters of the uncalibrated system together with the calibrated system with the proposed technique and with the average-method for all the angles in the measurement series. Fig. 14 depicts the PSL, which is almost constant throughout the whole FOV for the uncalibrated scenario. A significant reduction of the PSL is observed for both calibration methods, where the average-method tends to perform slightly better around boresight, but the proposed method greatly outperforms the average-method for angles above ±30° from boresight, i.e., $|\sin(\theta_0)| > 0.5$. Even if the PSL is reduced

with about 15 dB, the PSL is still approximately 10 dB above the theoretical PSL of the Hamming weighted ideal beam pattern.

Fig. 15 depicts the ISL, where the ISL of the uncalibrated data lies around −9 dB for most angles but increases to about −6 dB towards the larger angles. Similar to the PSL, both calibration methods perform well for all angles, reducing the ISL with about 11 dB for the average-method and 16 dB for the proposed method. Again, for large angles relative to boresight the proposed method performs significantly better with ISL values up to 10 dB lower than for the average-method. Like the PSL, the ISL is still not close to the theoretical Hamming weighted ISL after calibration. Again, this is a consequence of the low sidelobe levels of the window function, such that even very small inaccuracies of the calibration coefficients such as noise and discretization cause the relative sidelobe level to increase significantly.

C. CALIBRATION VARIATIONS

The proposed calibration technique increases the computational complexity because different calibration coefficients are applied to different DOA angles. In practice, this means that beamforming must be applied on an angle-by-angle basis, for instance with a backprojection algorithm. However, it is possible to reduce the computational complexity by applying the same coefficients for a broader angular frequency interval, either by averaging over a selection of angles or simply measure fewer sets of calibration coefficients. This will of cause decrease the beamforming performance, so in the end it becomes a matter of prioritization. For instance, the average calibration coefficients above 30°, below −30° and in the interval ±30° could be used, since the benefit of the proposed method is observed for large angles.

V. CONCLUSION

This paper presents a detailed model of the system imperfections in a MIMO radar system including both channel imbalances and mutual coupling. It is found that calibration of both types of system imperfections is necessary to achieve high performance of the MIMO radar within its whole FOV. Thus, a calibration technique has been presented, utilizing that a single MIMO measurement offers several observations of the relative radiation pattern of each channel to efficiently calibrate for the system imperfections. Calibration coefficients are estimated experimentally with an 8 × 8 X-band MIMO radar using open-ended waveguide antennas. An improvement of the peak sidelobe level and integrated sidelobe level of approximately 15 dB is found across the whole FOV. This corresponds to the achieved performance of another calibration method used for comparison at boresight. However, at large angles relative to the antenna boresight, the proposed calibration method performs particularly well even if the antennas are not minimum scatterers. This is an advantage for MIMO radar systems as they typically cover a wide FOV.

REFERENCES

[1] D. W. Bliss and K. W. Forsythe, "Multiple-input multiple-output (MIMO) radar and imaging: Degrees of freedom and resolution," in *Proc. 37th Asilomar Conf. Signals Syst. Comput.*, vol. 1, 2003, pp. 54–59.
[2] P. Stoica and J. Li, *MIMO Radar Signal Processing*. Hoboken, NJ, USA: Wiley, 2008.
[3] P. Stoica and J. Li, "MIMO radar with colocated antennas," *IEEE Signal Process. Mag.*, vol. 24, no. 5, pp. 106–114, Sep. 2007.
[4] R. Feger, C. Wagner, S. Schuster, S. Scheiblhofer, H. Jäger, and A. Stelzer, "A 77-GHz FMCW MIMO radar based on an SiGe single-chip transceiver," *IEEE Trans. Microw. Theory Techn.*, vol. 57, no. 5, pp. 1020–1035, May 2009.
[5] J. Klare, O. Biallawons, and D. Cerutti-Maori, "UAV detection with MIMO radar," in *Proc. Int. Radar Symp.*, 2017, pp. 1–8.
[6] S. Edelberg and A. A. Oliner, "Mutual coupling effects in large antenna arrays: Part 1—Slot arrays," *IRE Trans. Antennas Propag.*, vol. 8, no. 3, pp. 286–297, May 1960.
[7] J. H. Richmond, "A reaction theorem and its application to antenna impedance calculations," *IRE Trans. Antennas Propag.*, vol. 9, no. 6, pp. 515–520, Nov. 1961.
[8] J. L. Allen and B. Diamond, *Mutual Coupling in Array Antennas*, MIT Lincoln Lab., Lexington, MA, USA, 1966.
[9] J. B. Andersen and R. G. Vaughan, "Transmitting, receiving, and scattering properties of antennas," *IEEE Antennas Propag. Mag.*, vol. 45, no. 4, pp. 93–98, Aug. 2003.
[10] C. A. Balanis, *Antenna Theory, Analysis and Design*, 4th ed. Hoboken, NJ, USA: Wiley, 2016.
[11] D. F. Kelley and W. L. Stutzman, "Array antenna pattern modeling methods that include mutual coupling effects," *IEEE Trans. Antennas Propag.*, vol. 41, no. 12, pp. 1625–1632, Dec. 1993.
[12] D. M. Pozar, "The active element pattern," *IEEE Trans. Antennas Propag.*, vol. 42, no. 8, pp. 1176–1178, Aug. 1994.
[13] N. Colon-Diaz, J. G. Metcalf, D. Janning, and B. Himed, "Mutual coupling analysis for colocated MIMO radar applications using CEM modeling," in *Proc. IEEE Radar Conf. (RadarConf)*, 2017, pp. 441–446.
[14] G. Babur, P. J. Aubry, and F. Le Chavalie, "Antenna coupling effects for space-time radar waveforms: Analysis and calibration," *IEEE Trans. Antennas Propag.*, vol. 62, no. 5, pp. 2572–2586, May 2014.
[15] G. Babur, P. Aubry, and F. Le Chevalier, "Improved calibration technique for the transmit beamforming by a coherent MIMO radar with collocated antennas," in *Proc. 31st URSI Gen. Assembly Sci. Symp. (URSI GASS)*, 2014, pp. 1–4.
[16] C. M. Schmid, A. Stelzer, R. Feger, S. Schuster, and C. M. Schmid, "On the effects of calibration errors and mutual coupling on the beam pattern of an antenna array," *IEEE Trans. Antennas Propag.*, vol. 61, no. 8, pp. 4063–4072, Aug. 2013.
[17] B. T. Arnold and M. A. Jensen, "The effect of antenna mutual coupling on MIMO radar system performance," *IEEE Trans. Antennas Propag.*, vol. 67, no. 3, pp. 1410–1416, Mar. 2019.
[18] F. Belfiori, W. van Rossum, and P. Hoogeboom, "Array calibration technique for a coherent MIMO radar," in *Proc. 13th Int. Radar Symp.*, 2012, pp. 122–125.
[19] A. Durr *et al.*, "On the calibration of mm-Wave MIMO radars using sparse antenna arrays for DoA estimation," in *Proc. 16th Eur. Radar Conf.*, 2019, pp. 349–352.
[20] B. Friedlander and A. J. Weiss, "Direction finding in the presence of mutual coupling," *IEEE Trans. Antennas Propag.*, vol. 39, no. 3, pp. 273–284, Mar. 1991.
[21] I. J. Gupta and A. A. Ksienski, "Effect of mutual coupling on the performance of adaptive arrays," *IEEE Trans. Antennas Propag.*, vol. AP-31, no. 5, pp. 785–791, Sep. 1983.
[22] C. Zhang, H. Huang, and B. Liao, "Direction finding in MIMO radar with unknown mutual coupling," *IEEE Access*, vol. 5, pp. 4439–4447, 2017.
[23] H. Steyskal and J. S. Herd, "Mutual coupling compensation in small array antennas," *IEEE Trans. Antennas Propag.*, vol. 38, no. 12, pp. 1971–1975, Dec. 1990.
[24] C. M. Schmid, R. Feger, C. Wagner, and A. Stelzer, "Mutual coupling and compensation in FMCW MIMO radar systems," *Frequenz*, vol. 65, nos. 9–10, pp. 297–302, 2011. [Online]. Available: https://doi-org.proxy.findit.cvt.dk/10.1515/freq.2011.044

[25] C. M. Schmid, C. Pfeffer, R. Feger, and A. Stelzer, "An FMCW MIMO radar calibration and mutual coupling compensation approach," in *Proc. Eur. Microw. Week 10th Eur. Radar Conf.*, 2013, pp. 13–16.
[26] W. K. Kahn and H. Kurss, "Minimum-scattering antennas," *IEEE Trans. Antennas Propag.*, vol. 3, no. 5, pp. 671–675, Sep. 1965.
[27] B. Clerckx, C. Craeye, D. Vanhoenacker-Janvier, and C. Oestges, "Impact of antenna coupling on 2 × 2 MIMO communications," *IEEE Trans. Veh. Technol.*, vol. 56, no. 3, pp. 1009–1018, May 2007.
[28] J. B. Andersen and A. Frandsen, "Absorption efficiency of receiving antennas," *IEEE Trans. Antennas Propag.*, vol. 53, no. 9, pp. 2843–2849, Sep. 2005.
[29] P. Stoica and R. L. Moses, "Spatial methods," in *Spectral Analysis of Signals*. Upper Saddle River, NJ, USA: Pearson/Prentice Hall, 2005, pp. 263–319.
[30] D. M. Pozar, *Microwave Engineering*. New Delhi, India: Wiley, 2012.
[31] R. L. Grove and J. Dall, "On the impact of channel imbalance on MIMO radar performance," in *Proc. 17th Eur. Radar Conf. (EuRAD)*, 2021, pp. 330–333.

RICARD L. GROVE received the B.S. and M.S. degrees in electrical engineering within the Earth and Space Physics and Engineering Program from the Technical University of Denmark, Copenhagen, Denmark, in 2015 and 2017, respectively, where he is currently pursuing the Ph.D. degree in signal processing. His current research interests include system imperfection such as channel imbalance and mutual coupling on multiple-input multiple-output radars, the effects of the imperfections and calibration techniques to compensate for the imperfections.

JØRGEN DALL (Member, IEEE) received the M.Sc. degree in electrical engineering and the Ph.D. degree from the Technical University of Denmark in 1984 and 1989, respectively, where he is a Professor of Microwave Remote Sensing Systems. He has contributed to the development of the Danish airborne SAR, EMISAR, notably he led the development of a dedicated real-time SAR processor, was responsible for the offline data processing, and organized the EMISAR data acquisition campaigns in a five-year period. Later, he led the development of ESA's airborne Ice Sounding radar and SAR, POLARIS. Most recently, he led the development of an experimental X-band MIMO radar. His research interests include various aspects of ice sheet mapping using InSAR, PolInSAR, and TomoSAR techniques as well as ice sounding.

POUL LETH-ESPENSEN received the M.Sc. degree in electrical engineering and telecommunications from Aalborg University, Denmark, in 1994, where he was with Aalborg University, Center for Person Kommunikation as a Research Assistant and as an Assistant Research Professor from 1994 to 1998 and worked with signal processing and direction of arrival algorithms for speech signals and direction of arrival estimation algorithms in mobile phone antenna array systems. He joined TERMA A/S in 1998, where he has worked as an Electrical Engineer and as a Senior Engineer of Microwave Electronics, where he is currently a Specialist of Microwave Electronics. His current interests are microwave circuits and antennas.